5 ILLUSTRATIVE EXAMPLES

5.1 *Inverse Estimation of the Hardening Curve from the Tension Test*

5.1.1   The Tension Test

The tension test (Figure 5.1) is widely used for the mechanical testing of materials. However, accurate estimation of plastic material properties is difficult due to the non-uniform stress and strain distribution in the necking zone (Figure 5.2). Because of this phenomenon, it is not possible to determine the hardening parameters directly by measuring elongations at different loads. In order to determine true stress the Bridgeman correction is often applied which requires additional measurements of contractions at the narrowest part of the deformed sample and curvature of the neck[1]. The approach is based on the assumptions that the contour of the neck is the arc of a circle and that strains are constant over the cross section of the neck.

In the present section an inverse approach to estimation of hardening parameters is considered[2],[3]. This approach does not incorporate idealisations in the form of a priori assumptions on the stress or strain field. The material behaviour is modeled by a von Mises elasto-plastic material model[1].
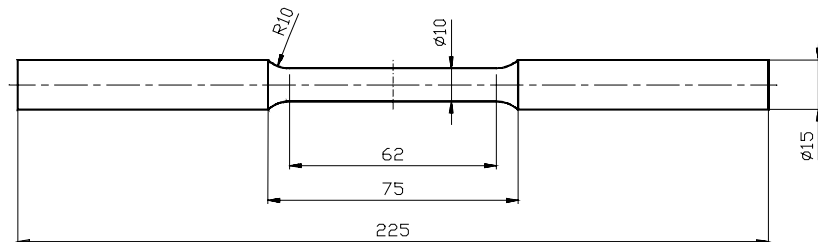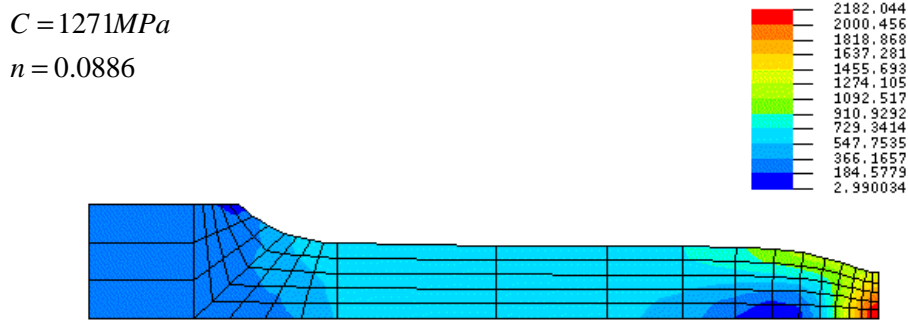

Figure 5.1: Sample geometry.

$C = 1271 MPa$

$n = 0.0886$

Figure 5.2: Longitudinal stress distribution obtained by numerical simulation. Exponential hardening law with $C = 1271 MPa$ and $n = 0.0886$ was assumed. The elongation is $8 mm$.

5.1.2 Estimation of an Exponential Approximation

An exponential hardening law is assumed to approximate the relationship between the effective stress and effective strain:

$$\bar{\sigma} = C\bar{\varepsilon}^n \ . \tag{5.1}$$

The unknown parameters C and n need to be derived from measured forces at certain elongations of the samples. Two series of measurements were performed for two different steel grades. The geometry of the samples is shown in Figure 5.1, while the experimental data are given in Table 5.1 and Table 5.2 for each series. Graphic presentation of the same data for the first sample of each series is given in Figure 5.3.

Table 5.1: Experimental data for the first series.

Elongation [mm]	Force [N], sample 1	Force [N], sample 2	Force [N], sample 3
3	65900	68800	66800
4	67800	69900	67800
5	68650	70600	68700
6	68900	70600	68700
7	68850	69200	68400
8	68000	66600	68200

| 9 | 65800 | 61300 | 65100 |
| 10 | 61800 | 54100 | 59300 |

Table 5.2: Experimental data for the second series.

Elongation [mm]	Force [N], sample 1	Force [N], sample 2	Force [N], sample 3
3	86000	85800	84700
4	87500	86300	85600
5	87800	86500	86400
6	86500	85900	84500
7	81700	84600	80900
8	74800	78200	72600
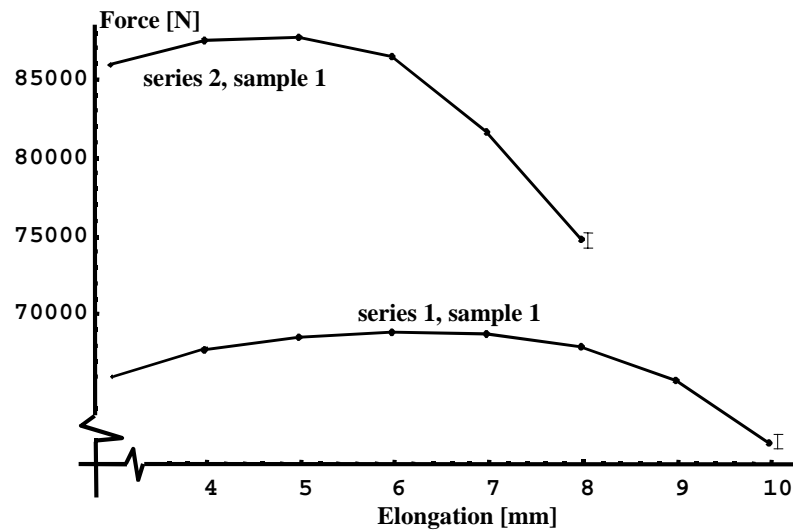
Figure 5.3: Measured data for the first sample of each series.

Solution of the problem was found by searching for the parameters which give the best agreement between measured and respective numerically calculated quantities. The agreement can be defined in different ways, but most commonly used is the least-square concept, mostly because of its statistical background[21]-[23]. The problem is solved by minimising the function

$$\chi^2(C,n) = \sum_{i=1}^{N} \frac{\left(F_i^{(m)} - F_i(C,n)\right)^2}{\sigma_i^2} \ , \tag{5.2}$$

where $F_i^{(m)}$ are measured forces at different elongations, $F_i(C, n)$ are the respective quantities calculated with the finite element model by assuming trial values of parameters C and n, σ_i are the expected errors of appropriate measurements and N is the number of measurements.

The scatter of experimental data for the same series which is evident from Table 5.1 and Table 5.2 is mainly due to differences in samples rather than experimental errors. This has an effect on the estimated parameters C and n. The results are summarized in Table 5.3 and Table 5.4.

Table 5.3: Calculated parameters C and n for the first series.

	sample 1	sample 2	sample 3
$C[MPa]$	1271	1250	1258
n	0.1186	0.1010	0.1132

Table 5.4: Calculated parameters C and n for the second series.

	sample 1	sample 2	sample 3
$C[MPa]$	1492	1511	1462
n	0.08422	0.09269	0.08318

It seems that the applied numerical model simulates the bahaviour of the investigated material adequately. This is indicated[22],[24] by the fact that the obtained minimal values of the function $\chi^2(C, n)$ were never much greater than one, assuming that the measurement errors (σ_i in (5.2)) are one percent of the related measured values.

## 5.1.3   Estimation of a Piece-wise Linear Approximation

The flow stress of the material is a result of different hardening and softening phenomena which interact during plastic deformation. This interaction is often so

complex that it is difficult to predict the form of the hardening curve $\overline{\sigma}(\overline{\varepsilon})$. In such cases it would be desirable to find an approximation of the hardeining curve without making any preassumptions regarding its form. This can be done in several ways. In this work, an approach where points of the hardening curve defining a piece-wise linear approximation are sought is considered.

The experimental measurements used for estimation of the piece-wise linear approximations are summarized in Table 5.5 and Figure 5.4. The data are for the first sample of the first series, but with 16 measurements instead of eight used for evaluation of exponential approximation.

Table 5.5: Experimental data used to obtain a piece-wise linear approximation of the hardening curve.

| Elongation [mm]	Force [N]
2	62200
2.5	64400
3	65900
3.5	67000
4	67800
4.5	68200
5	68650
5.5	68800
6	68900
6.5	69000
7	68850
7.5	68600
8	68000
8.5	67100
9	65800
9.5	64000
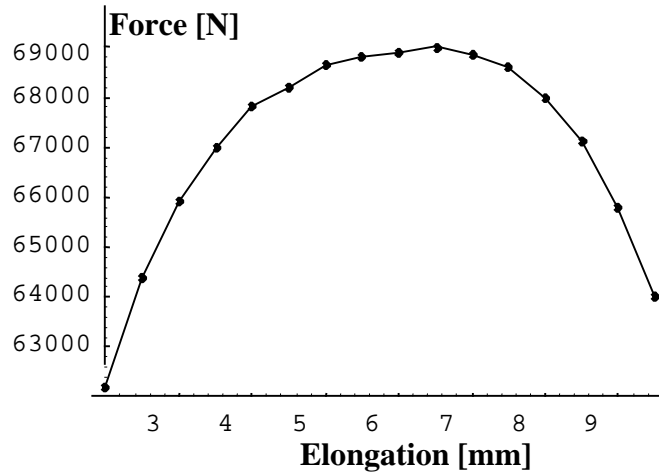
Figure 5.4: Measurements used for calculating a piecewise approximation of the hardening curve (measurements are for the first sample of the first series).

The points on the hardening curve were obtained by minimising the function

$$\chi^2\left(\overline{\sigma}_1,\overline{\sigma}_2,...,\overline{\sigma}_M\right)=\sum_{i=1}^{N}\frac{\left(F_i^{(m)}-F_i\left(\overline{\sigma}_1,\overline{\sigma}_2,...,\overline{\sigma}_M\right)\right)^2}{\sigma_i^2}\,,\tag{5.3}$$

where parameters $\overline{\sigma}_i$ are values of the curve $\overline{\sigma}(\overline{\varepsilon})$ at arbitrary equivalent strains $\overline{\varepsilon}_i$. The yield stress was known from experiments.
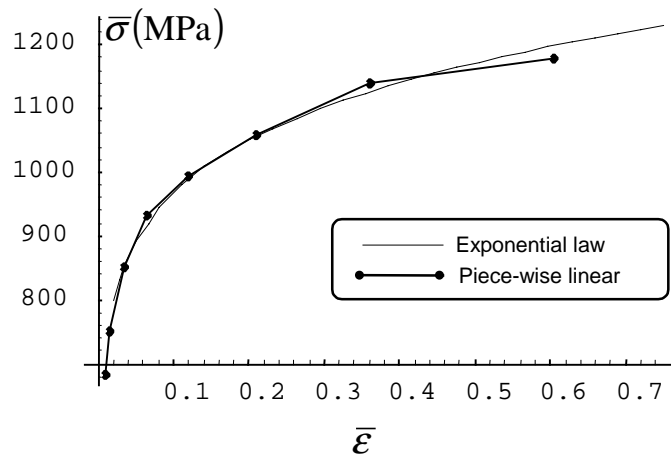
Approximations of the hardening curve with 4, 6, 8 and 10 points were calculated. The results are shown in Figure 5.5 to Figure 5.8. The exponential hardening curve with parameters $C=1271\,MPa$ and $n=0.1186$ (as obtained by the inverse analysis assuming the exponential hardening law) is drawn in each figure for comparison. It is evident from these graphs that calculated piecewise linear approximations are in relatively good agreement with the calculated exponential approximation.
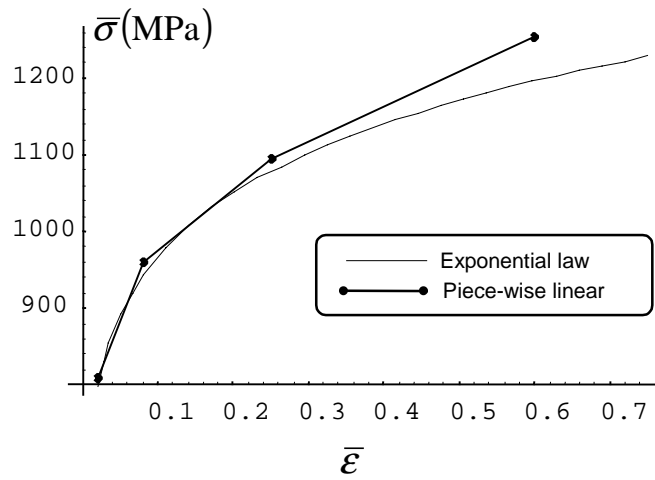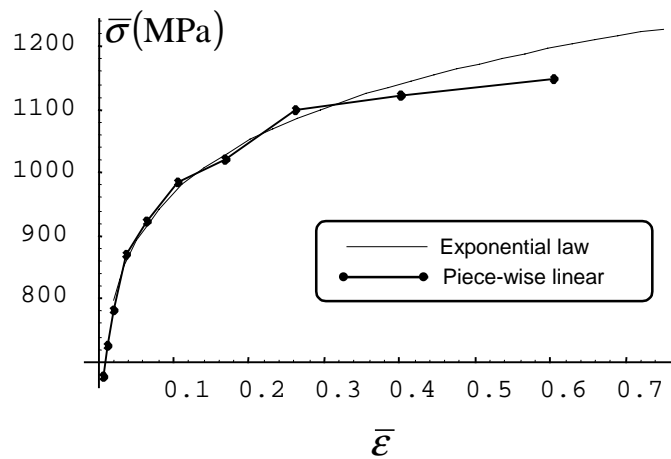
Figure 5.5: Comparison between exponential and piece-wise linear (4 points) approximations of the hardening curve.
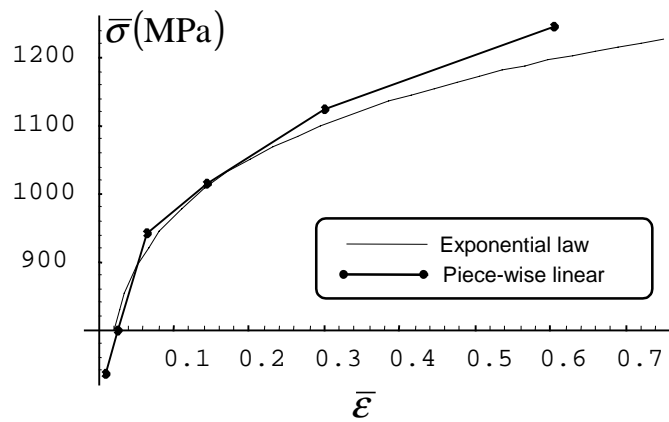
Figure 5.6: Comparison between exponential and piece-wise linear (6 points) approximations of the hardening curve.

Figure 5.7: Comparison between exponential and piece-wise linear (8 points) approximations of the hardening curve.


Figure 5.8: Comparison between exponential and piece-wise linear (10 points) approximations of the hardening curve.

5.1.4   Numerical Tests

A number of numerical tests were performed to investigate the stability and uniqueness of the inverse solutions for the exponential approximation of the hardening curve.

181

Several inverse analyses were performed with very different initial guesses and they always converged to the same results. This is the first indication that the problem is not ill-posed. Further examination was made by plotting the χ^2 function (Figure 5.9 and Figure 5.10). A distinctive minimum can be recognised in these figures without indication of possible existence of several local minima.
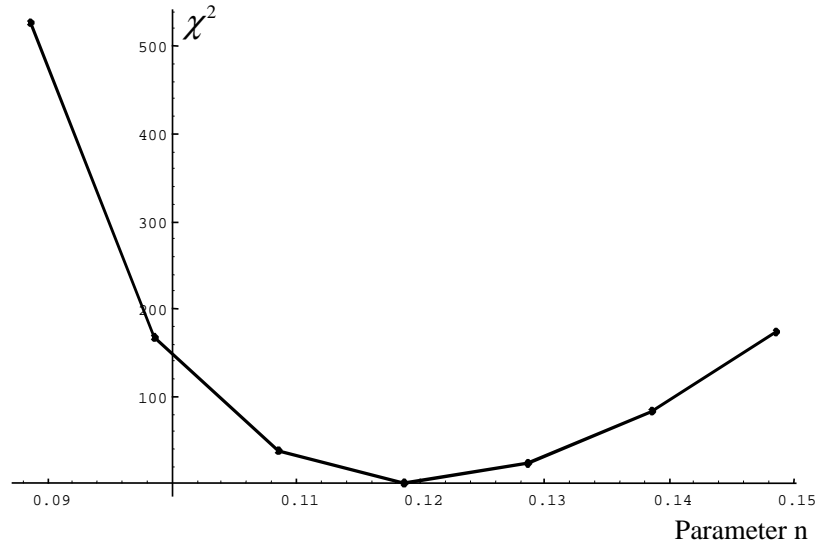
Figure 5.9: Dependence of function χ^2 on parameter n at measured data for sample 1 of series 1. Parameter C is set to 1271 MPa.
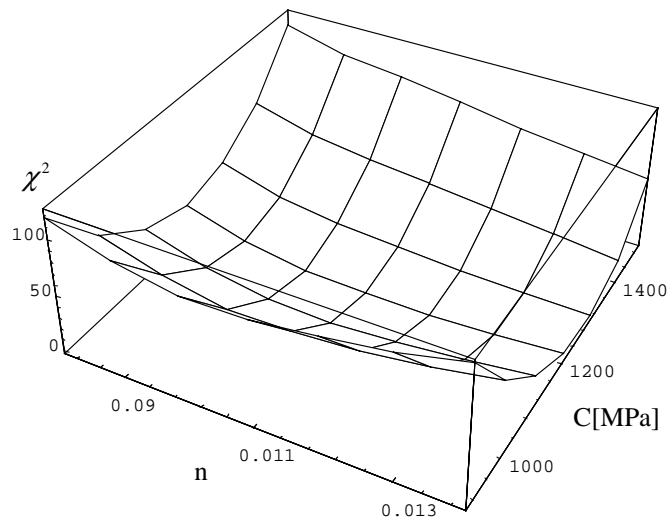
Figure 5.10: Dependence of function χ^2 on both parameters for the same measured data as in Figure 5.3.

To test the stability of the solutions, a Monte Carlo simulation[11] was performed. It was assumed that the correct values of both parameters were known. For this purpose, the previously calculated values for the first sample of the first series were taken, namely $C = 1271\ MPa$ and $n = 0{,}1186$ (see Table 5.1). With these values the so called "exact measurements" $F_i^{(0)}$ were obtained with the same finite element model used for the inverse analysis of the real measurements. The "simulated measurements" $F_i^{(m)}$ were successively obtained by adding random errors r_i to the "exact measurements". Errors were distributed normally as

$$\frac{d\,P}{d\,r_i} = \frac{1}{\sqrt{2\,\pi}}\,exp\!\left(-\frac{r_i^2}{2\,s_i^2}\right)\,, \tag{5.4}$$

where s_i is the standard deviation of distribution. This distribution is often used to simulate measurement errors which do not have a clearly defined origin[22].

For each set of "simulated measurements" parameters C and n were calculated. Three different sets of s_i were chosen so that ratios

$$R_i = \frac{s_i}{\left|F_i^0\right|} \tag{5.5}$$

were uniform within each set. Fifty numerical experiments were performed for $R = 0.01$, twenty for $R = 0.1$ and twenty for $R = 0.001$. Then average values $\bar{z}$ and dispersions S_z of the searched parameters were calculated for each set, according to

$$\bar{z} = \frac{1}{k}\sum_{i=1}^{k} z_i \tag{5.6}$$

and

$$S_z^2 = \frac{1}{k-1}\sum_{i=1}^{k}\left(z_i - \bar{z}\right)^2\,. \tag{5.7}$$

The results are summarized in Table 5.6. Figure 5.11 shows the distribution of calculated parameters at $R = 0.01$.
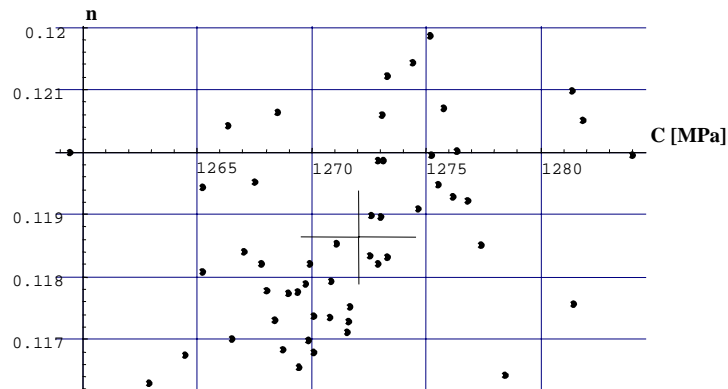
Figure 5.11: Results of the Monte carlo simulation for $R = 0.01$.

Table 5.6: Results of Monte Carlo simulations: Average values and dispersions of calculated parameters at different R_i

	$R = 0{,}001$	$R = 0{,}01$	$R = 0{,}1$
$\overline{C}$	1271.4	1271.8	1287
S_C	0.58	4.9	69
$\overline{n}$	0.118628	0.11867	0.1163
S_n	0.00016	0.0015	0.014

5.1.5   Concluding Remarks

The above example illustrates the applicability of the inverse approach in parameter identification. Inverse identification can become a useful tool for estimation of those parameters which are difficult to obtain with analytical treatment of experimental results due to the complexity of the phenomena involved. An important advantage of the approach is that parameters are derived by using the same numerical model which is then applied in direct simulations.

It is necessary to take the appropriate precautions when the approach is used. It is especially necessary to make sure that the inverse problems is well conditioned and has a unique solution. If measurement errors can be estimated, then statistical tests can be used to verify the adequacy of the applied model and estimated

parameters. It is wise to use the estimated parameters in additional tests where simulation results are compared with measurements.

5.2 Shape Optimisation of Cold Forging Processes

Two simple examples are included to illustrate the applicability of the optimisation techniques in the design of forming processes. In the first example a pre-form of a cold forged workpiece is optimised in order to obtain the desired final form. In the second example the shape of the tool in the first stage of a two stage cold forging process is optimised with the same objective. These examples explain the methodology which could be applied in the optimisation of real processes.

5.2.1   Optimisation of Preform Shape

In the present example an axisymmetric workpiece is upset by flat tools (Figure 5.1) with a constant stroke. The optimisation objective is to achieve a prescribed shape of the free boundary of the workpiece by changing the initial shape of this boundary. The Von Mises elasto-plastic material model was used for the workpiece while the tool was modelled as a rigid body. The coulomb friction law was used to model the contact condition between the die and the tool. Because of symmetry the process was modelled in two dimensions.
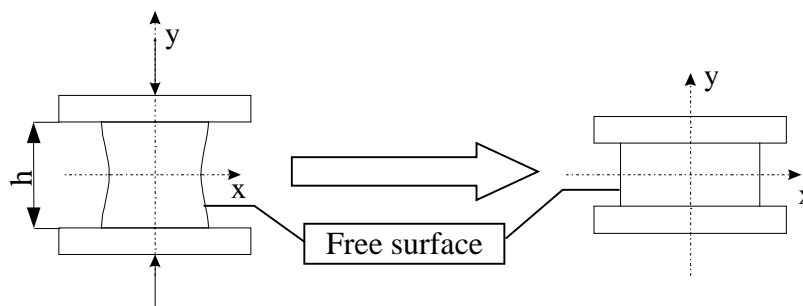
Figure 5.12: The forming Process.

The initial height (h=100 mm) of the workpiece was reduced by 40 per cent. The desired shape of the free edge was specified by a function prescribing the dependency of x position on y position of the nodes on the free boundary, i.e.

$$x_i = f(y_i) \quad i = 1,..,N , \tag{5.8}$$

where N is the number of nodes on the free boundary. Two different final shapes were prescribed:

$$f(y_i) = R = 1.3 \, h \tag{5.9}$$

and

$$f(y_i) = R + \cos\left(\frac{\pi y_i}{40 \, mm}\right)\cos\left(\frac{\pi y_i}{150 \, mm}\right) \tag{5.10}$$

The problem was solved by minimisation of the following objective function:

$$\chi^2(\mathbf{p}) = \sum_{i=1}^{N} \left((x_i(\mathbf{p}) - f(y_i(\mathbf{p})))\right)^2 . \tag{5.11}$$

$\mathbf{p}$ is the vector of optimisation parameters which describe the initial free boundary shape and x_i and y_i are the final positions of these nodes.

The initial free boundary shape was parametrised by polynomial Lagrange interpolation[23]

$$x = P(\mathbf{p}, y) \tag{5.12}$$

on a given number of control points equidistantly distributed in the y direction between the lowest and the highest point of the workpiece (including the extreme points). The x coordinates of the control points represented optimisation parameters p_i. Optimisation parameters (i.e. coefficients of the interpolation polynomial) determined the initial positions of nodes on the free boundary:

$$x_i^0 = P(\mathbf{p}, y_i^0), \; i = 1,...,N , \tag{5.13}$$

The Lagrangian interpolation is defined with[23]

$$L(p_1, p_2, ..., p_M, y) = \sum_{k=1}^{M} p_k L_k(y), \qquad (5.14)$$

where

$$L_k(p_1, ..., p_M, y) = \frac{(y - p_1)...(y - p_{k-1})(y - p_{k+1})...(y - p_M)}{(p_k - p_1)...(p_k - p_{k-1})(p_k - p_{k+1})...(p_k - p_M)} \qquad (5.15)$$

and M is the number of parameters. The control points lie on the interpolation polynomal, therefore parameters which are the x coordinates of these points have a geometrical interpretation.

Table 5.1 summarises the optimisation results. The results are shown graphically in Figure 5.13 and Figure 5.14. The quantity

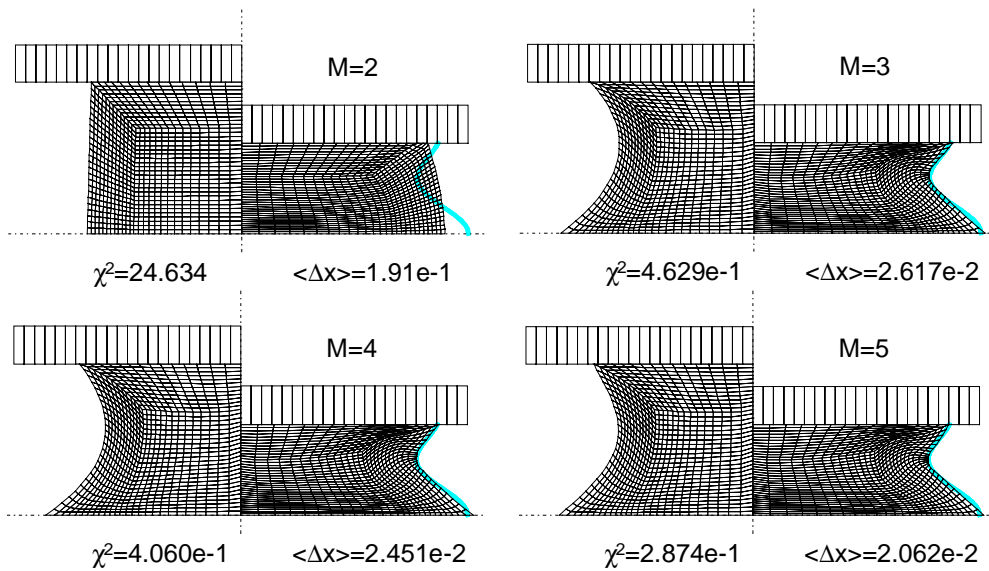$$< \Delta x > = \frac{\sqrt{\chi^2}}{N} \qquad (5.16)$$

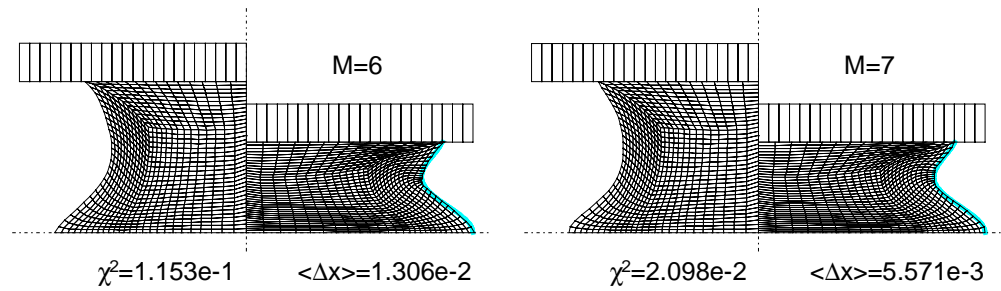was introduced in order to make comparison of the results more evident.

Table 5.7: Results of optimisation for required flat boundary defined by (5.9) and for the required curved boundary defined by (5.10) for different numbers of parameters.

M	Flat boundary required		Curved boundary required	
	χ^2[mm^2]	$<\Delta x>$[mm]	χ^2[mm^2]	$<\Delta x>$[mm]
2	0,1072244	0,0125943	24,6340628	0,1908951
3	0,0114715	0,0041194	0,4628830	0,0261675
4	0,0000310	0,0002143	0,4060472	0,0245084
5	0,0000033	0,0000700	0,2874089	0,0206194
6			0,1152899	0,0130594
7			0,0209804	0,0055710

χ^2=1.072e-1   <Δx>=1.259e-2 χ^2=1.147e-2   <Δx>=4.119e-3

χ^2=3.1e-5   <Δx>=2.143e-4 χ^2=3.3e-6   <Δx>=7.0e-5
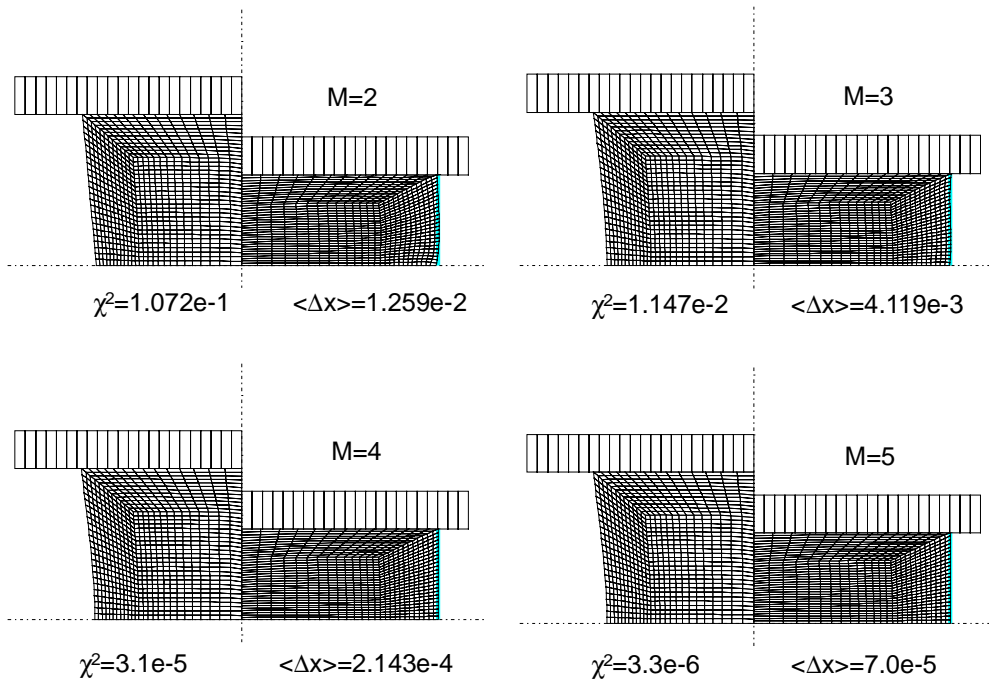
Figure 5.13: Comparison of solutions for the required flat free boundary defined by (5.9). The initial finite element mesh is depicted on the left hand side and the mesh after the forming process on the right hand side of each graph.

χ^2=24.634   <Δx>=1.91e-1 χ^2=4.629e-1   <Δx>=2.617e-2

χ^2=4.060e-1   <Δx>=2.451e-2 χ^2=2.874e-1   <Δx>=2.062e-2

M=6   M=7

$\chi^2=1.153e-1$ $<\Delta x>=1.306e-2$ $\chi^2=2.098e-2$ $<\Delta x>=5.571e-3$
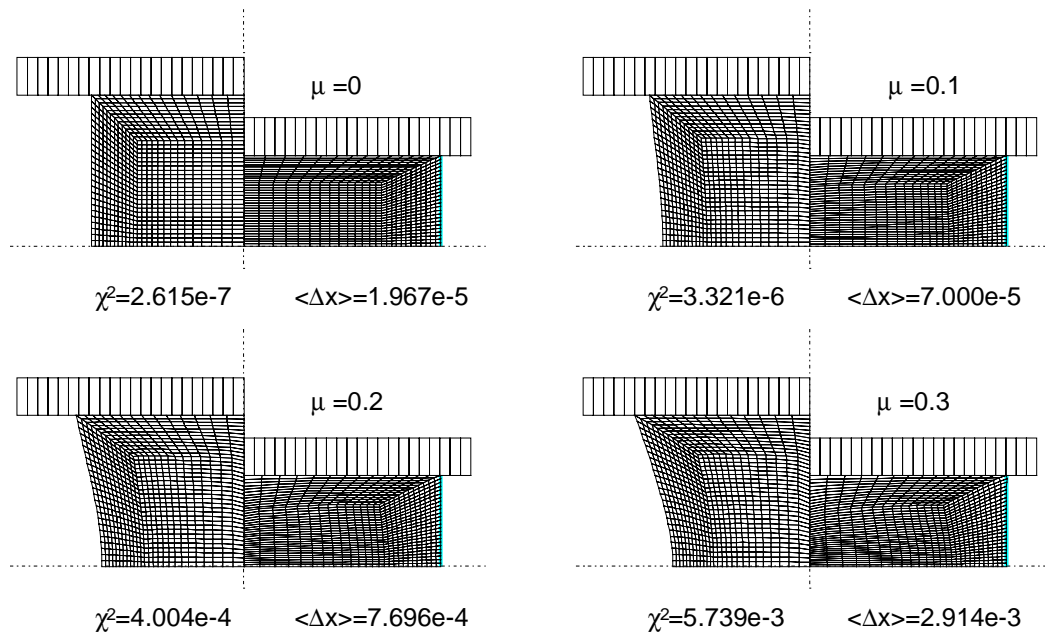
Figure 5.14: Comparison of solutions for the required curved free boundary defined by (5.10).

The above results were obtained with a friction coefficient $\mu = 0.1$ between the tool and the workpiece. The friction coefficient plays an important role in the process, therefore its influence was analysed. Figure 5.15 shows the simulation of the process with different friction coefficients, where the optimal initial shape of the optimisation problem with a required flat boundary was adopted as the initial geometry of the workpiece. Figure 5.16 shows the optimal initial shapes for this problem with different values of the friction coefficient.

$\mu = 0$ $\mu = 0.1$

$\mu = 0.2$ $\mu = 0.3$
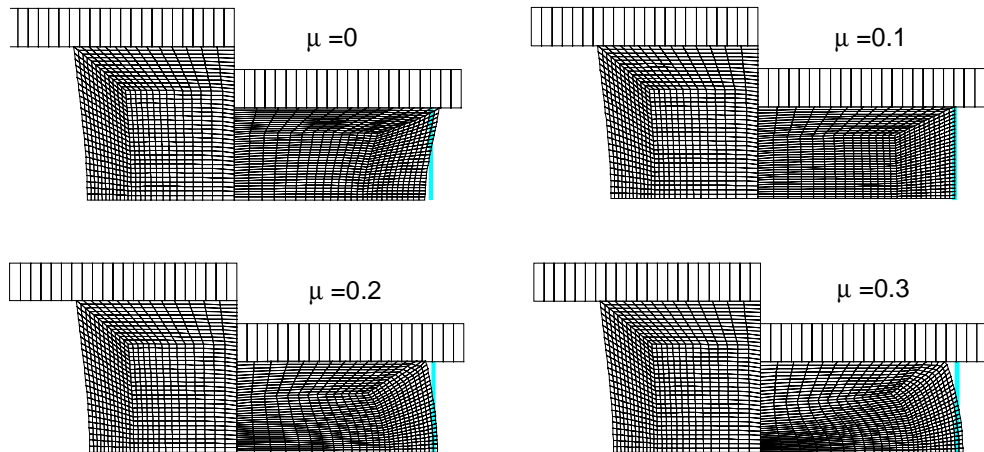
Figure 5.15: Simulation of the process with different values of friction coefficient μ. The process starts with the optimal initial shape for $\mu = 0.1$ and required flat free boundary.

$\chi^2=2.615\text{e-}7$ $<\Delta x>=1.967\text{e-}5$ $\chi^2=3.321\text{e-}6$ $<\Delta x>=7.000\text{e-}5$

$\chi^2=4.004\text{e-}4$ $<\Delta x>=7.696\text{e-}4$ $\chi^2=5.739\text{e-}3$ $<\Delta x>=2.914\text{e-}3$
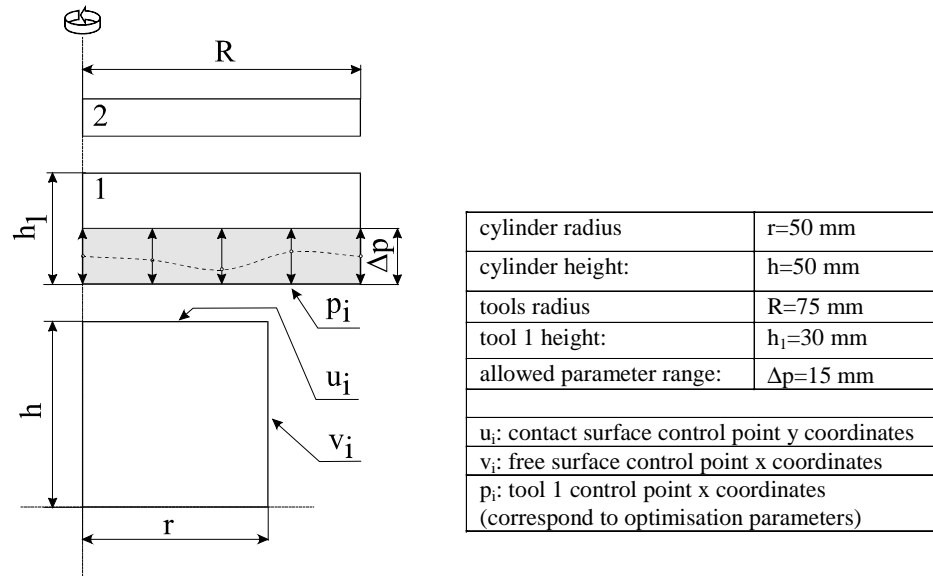
Figure 5.16: Solution of the optimisation problem with different friction coefficients μ.

5.2.2   Shape Optimisation of a Tool in a Two Stage Forging

In the previous example the shape of the forged workpiece was optimised with the aim of achieving the desired final shape. In multi stage forging processes the shape of the workpiece is obtained by the preceeding operation in the forging sequence. This situation is illustrated by the following example where the tool shape for the first of the two forging operations is optimised in order to achieve the desired final shape of the workpiece.

The optimised process is outlined in Figure 5.17. In the first stage the axisymmetric workpiece is forged by a tool with curved boundary. In the second stage the workpiece is forged by a flat tool with the stroke corresponding to the final height reduction of 40 per cent. The same material model as in the previous example was assumed.

cylinder radius	r=50 mm
cylinder height:	h=50 mm
tools radius	R=75 mm
tool 1 height:	h₁=30 mm
allowed parameter range:	Δp=15 mm
u_i: contact surface control point y coordinates	
v_i: free surface control point x coordinates	
p_i: tool 1 control point x coordinates (correspond to optimisation parameters)	

Figure 5.17: Outline of the optimised process.

The objective of optimisation was to find such a shape of the first tool that both the contact surface and free boundary of the workpiece are flat after the second stage. This was achieved by minimisation of the following objective function:

$$D(\mathbf{p}) = D(\mathbf{u}(\mathbf{p}), \mathbf{v}(\mathbf{p})) = D_u + D_v = \sum_{i=1}^{M} \frac{(u_i - \bar{u})^2}{\bar{u}^2} + \sum_{i=1}^{N} \frac{(v_i - \bar{v})^2}{\bar{v}^2}, \qquad (5.17)$$

where

$$\bar{u} = \sum_{j=1}^{M} \frac{u_j}{M}, \qquad (5.18)$$

$$\bar{v} = \sum_{j=1}^{N} \frac{v_j}{N}, \qquad (5.19)$$

M is the number of control points (nodes) on the contact surface of the workpiece, N is the number of control points on the free surface of the workpiece, and the meaning of other quantities is evident from Figure 5.17. The dependence of u_i and v_i on optimisation parameters $\mathbf{p}$ was suppressed for clarity.

The shape of the contact surface of the first tool was parametrised with 3rd order splines in such a way that optimisation parameters correspond to y coordinates of the equidistant control points defining the splines.

In order to avoid physically infeasible situations, the range of parameters p_i was limited to an interval of the height Δp (Figure 5.17). This was achieved by introducing new variables[4] t_i and defining the transformation F that maps t_i to p_i, in the following way:

$$p_i = F(t_i) = \tfrac{1}{2}(p_{\min} + p_{\max}) + \tfrac{1}{\pi}(p_{\max} - p_{\min})\,arctg(t_i), \qquad (5.20)$$

where $p_{\min}$ and $p_{\max}$ are lower and upper bounds for parameters p_i, respectively. The transformation F maps the interval $(-\infty, \infty)$ to $(p_{\min}, p_{\max})$. The objective function defined in the space of parameters t_i, i.e.

$$\tilde{D}(\mathbf{t}) = D(\mathbf{p}(\mathbf{t})), \qquad (5.21)$$

was minimised with respect to these parameters. Results are summarised in Table 5.8. Parameters p_i in the table are scaled with respect to $h_1 = 30\,mm$. Five shape parameters were used, while p_6 denotes the tool stroke. The first row of the table contains results for the process performed with the flat tool in the first stage. The second row contains results for the optimised shape with a constant stroke in the first stage (20 mm). The third row contains results for the case where the stroke of the tool in the first stage is taken as the sixth parameter. The corresponding forging sequences are shown in Figure 5.18 to Figure 5.20

Table 5.8: Optimal parameters and values of the objective function.
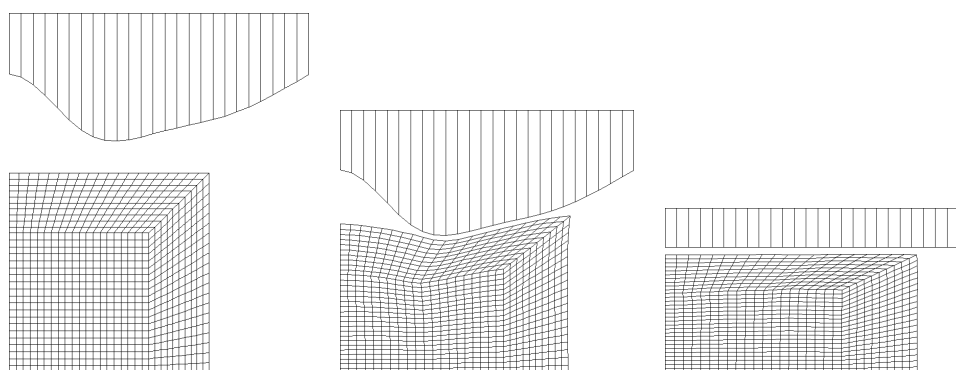
	p_1	p_2	p_3	p_4	p_5	p_6	D_u	D_v	D
1	1	1	1	1	1	2/3	1.063E-4	7.927E-3	8.033E-3
2	0.506	0.992	0.991	0.539	0.509	2/3	1.67E-04	2.61E-04	4.28E-04
3	0.506	0.991	0.992	0.832	0.51	0.832	1.30E-04	1.49E-05	1.44E-04
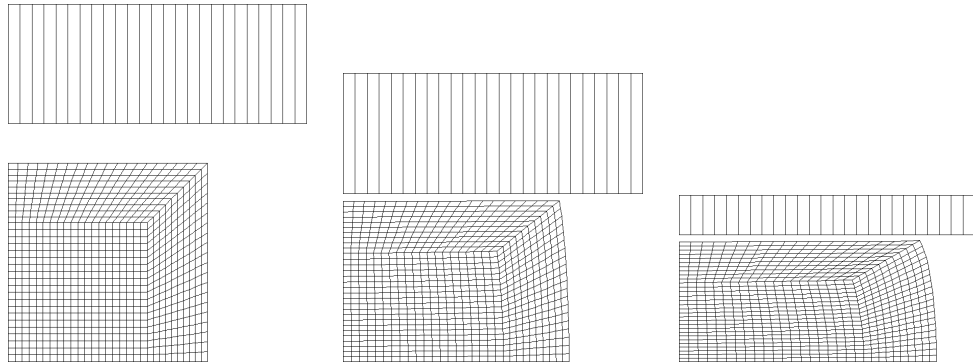
Figure 5.18: Forging process with a flat tool.
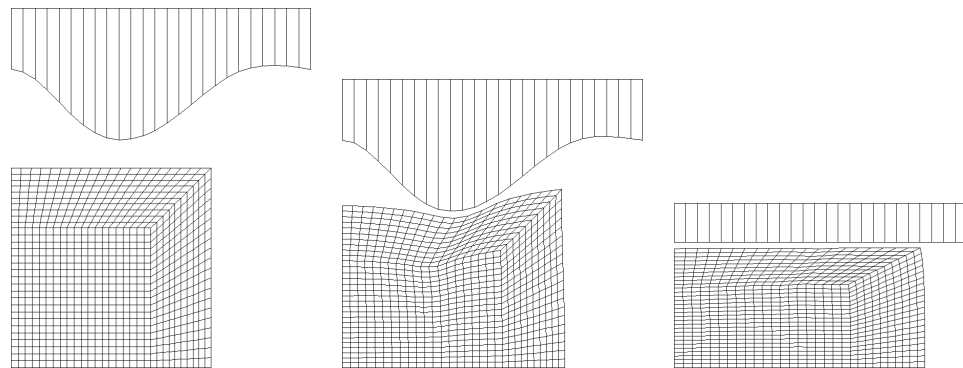
**Figure 5.19:** Forging process with an optimised tool shape and a prescribed stroke.

Figure 5.20: Forging process with an optimised tool shape, where the stroke was taken as a parameter.

### 5.2.3   Optimisation of Heating Parameters for Hot Forming Operation

In the present example a two stage forming process is considered. In the first stage (heating, Figure 5.21) an axisymmetric billet with length $L=30$ *mm* and radius $r=10$ *mm* with initial temperature 20 *°C* is heated at $x=L$ with a heat flux F_o for time t_h while the surface at $x=0$ is kept at the initial temperature. Other surfaces are insulated.

In the second stage (forming, Figure 5.22) the billet is deformed in such a way that the prescribed displacement at $x=L$ is $u_x=-2$ *mm* and at $x=0$ is $u_x=0$. Other surfaces are free. The deformation is modelled by an ideal elasto-plastic material model where the flow stress depends on temperature. No heat transfer is assumed in the second stage.

Material properties are summarised in Table 5.9 and Table 5.10. Figure 5.21 and Figure 5.22 show the discretised configurations of the specimen before and after heating and forming. Only half of the domain is represented due to symmetry.
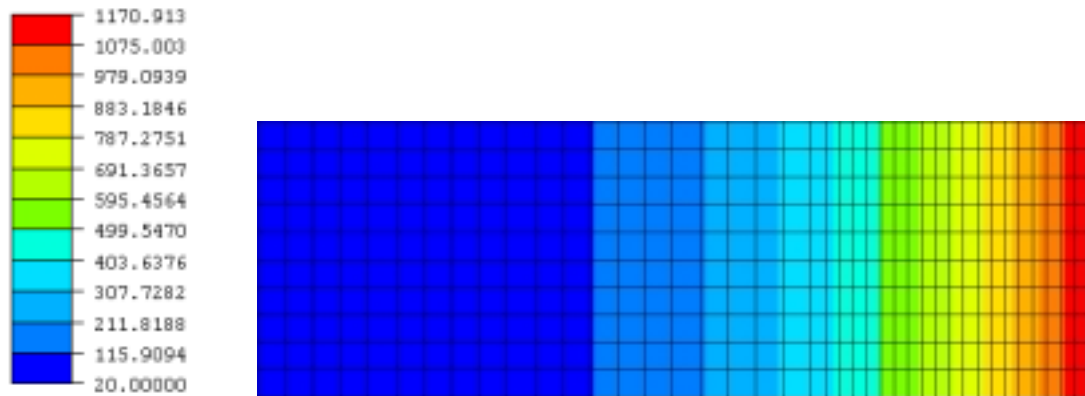
Figure 5.21: Temperature distribution after heating. The heat flux $F_o=3.500$ W/m^2 is applied for $t_h=10$ s.
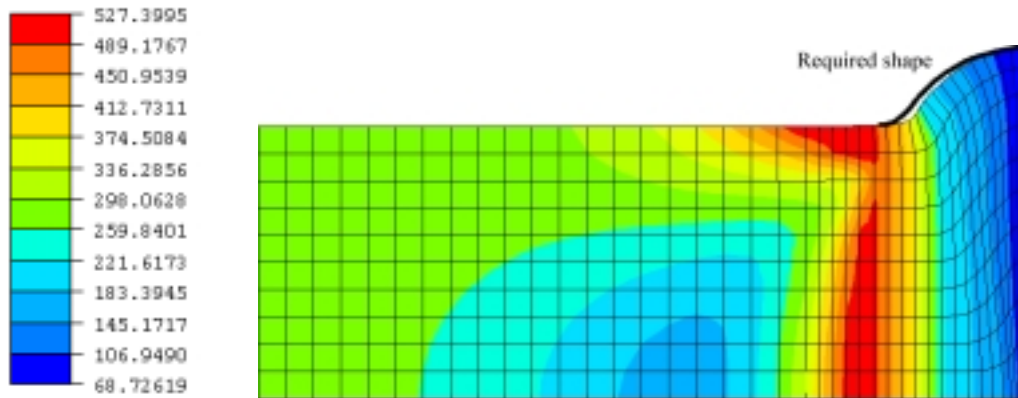
Figure 5.22: Effective stress distribution in the deformed specimen after forming. Displacement of the right surface is $u_x = -2$ mm.

Table 5.9: Material properties.

Thermal conductivity (K)	30 W/mK
Heat capacity (C)	500 J/kg K
Density (ρ)	7850 kg/m^3
Youngs modulus (E)	210000 MPa
Poissons ratio (ν)	0.3

Table 5.10: Yield stress as a function of temperature.

Temperature [^{o}C]	Yield stress [MPa]
20	700
100	620
200	560
300	540
400	510
500	500
600	390
700	200
800	180
900	150
1000	120
1100	90
1200	60

The aim is to find optimal heating parameters defined by heat flux F_o and heating time t_h so that the difference between the required and computed shapes of the specimen after forming is minimal. The objective function to be minimised is expressed in terms of the differences of the required and computed node coordinates in the interval $20mm \leq x \leq 28mm$. The choice of heating parameters is constrained by a maximum permissible temperature of the specimen $T_{max}=1200^{\circ}C$. The constraint is presented in Figure 5.23.
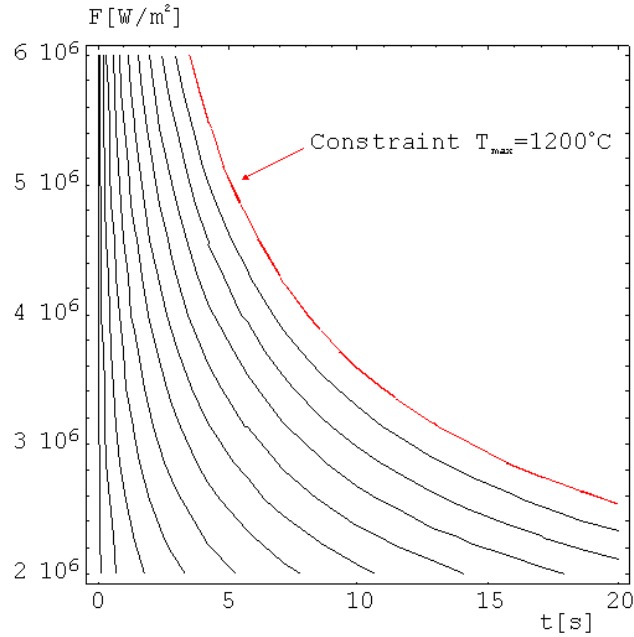
Figure 5.23: Constraint imposed on the choice of heating parameters. Contours show maximum temperature of the specimen as a function of applied heat flux and heating time. Spacing between contours is $100^{\circ}C$

The constraint is implied by adding a penalty term in the objective function:

$$D(\mathbf{p}) = \sum_{i=1}^{N} \left(y_i^p - y_i^m(\mathbf{p}) \right)^2 + C \exp\left(T(\mathbf{p}) - T_{max} \right) \tag{5.22}$$

$\mathbf{p} = [F_0, t_h]^t$ is the vector of optimisation parameters. The nodal coordinates prescribed by the required final shape are denoted by upper index p and the nodal coordinates calculated at given values of optimisation parameters are denoted by upper index m. The temperature at the right-hand end of the billet after heating is denoted by $T(\mathbf{p})$.

The heat flux and heating time can only have positive values. This is ensured by applying a transformation function that maps parameters from [-∞,∞] to [0,∞]:

$$p_i = G(q_i) = A\exp(Bq_i),\ \ i=1,2. \tag{5.23}$$

The billet deformation after the forming depends on the billet temperature distribution, which is calculated according to the following equation[20],[22]:

$$T(x,F,t) = \frac{Fx}{K} - \frac{8Fl}{K\pi^2}\sum_{n=1}^{\infty}\left(\frac{(-1)^n}{(2n+1)^2}\exp(-\frac{K(2n+1)^2\pi^2 t}{\rho C4l^2})\right)\sin\left(\frac{(2n+1)\pi x}{2l}\right) \tag{5.24}$$

Temperature distributions for three different heating regimes are presented in Figure 5.24.
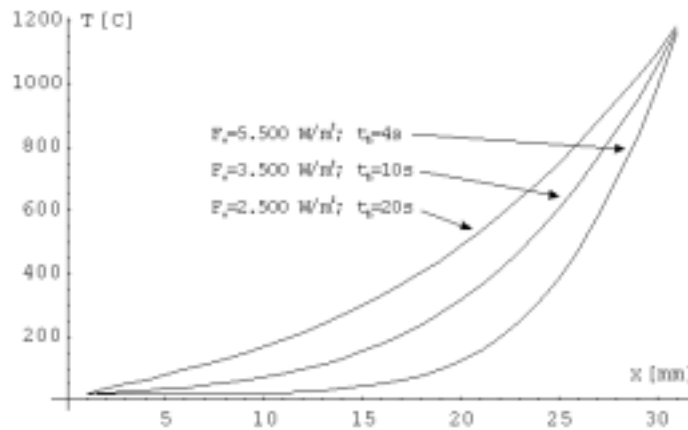
Figure 5.24: Temperature distributions along the x axis for three different heating regimes.

Different temperature distributions result in different shapes of the billet after the forming. Shapes that correspond to temperature distributions from the Figure 5.24 are presented in Figure 5.25.
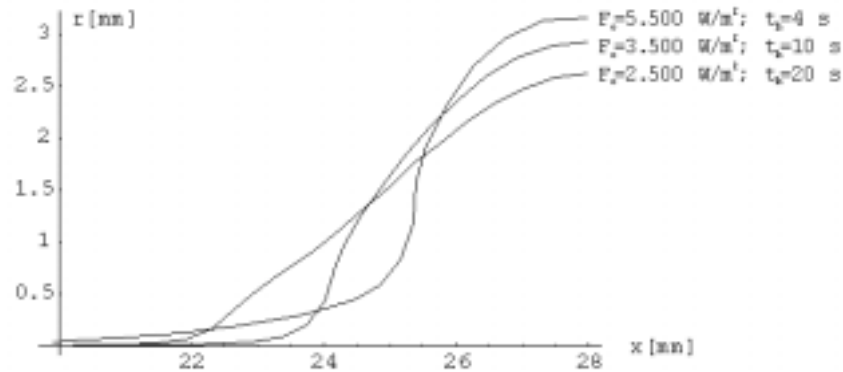
Figure 5.25: Deformed shapes of the specimen after forming for three different heating regimes from Figure 5.24.

The required shape of the billet after both stages of forming was prescribed by the following function:

$$y^p(x) = r + \frac{3}{1 + 25000\exp(-2(x - 20))}.$$ (5.25)

Optimisation was done by the inverse shell using the nonlinear simplex method. Optimal solution was found in 34 iterations. The required shape and the shape achieved with optimal parameters are shown in Figure 5.26.
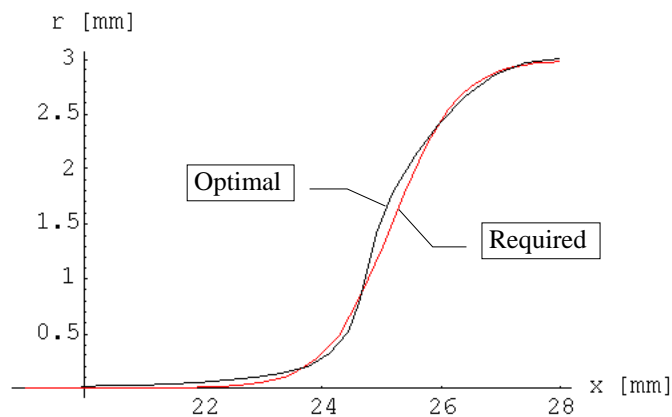

Figure 5.26: Required and optimal shape of the billet at optimal parameter values $F_{opt} = 3628674.9$ W/m^2 and $t_{opt} = 7.99$ s. Value of the objective function at these parameters was D($\mathbf{p}_{opt}$) = 0.1448.

The optimisation shell tabulating utilities were employed to sample the objective function in the neighbourhood of optimal parameters. Sampled data was plotted by *Mathematica*. Figure 5.27 shows 19x17 points diagram of the objective function without the penalty term. In Figure 5.28 the constraints, the optimisation path and the optimal solution are also shown.
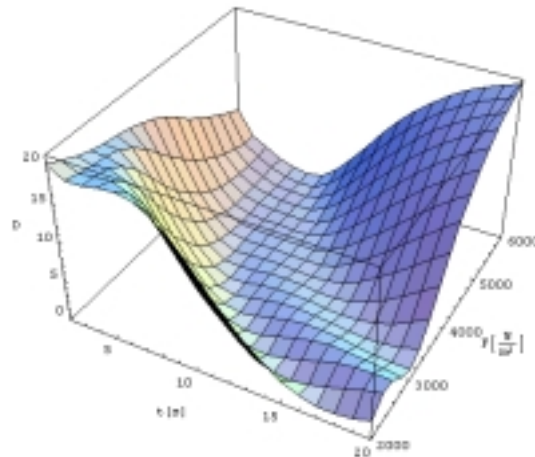
Figure 5.27: Objective function without the penalty term.
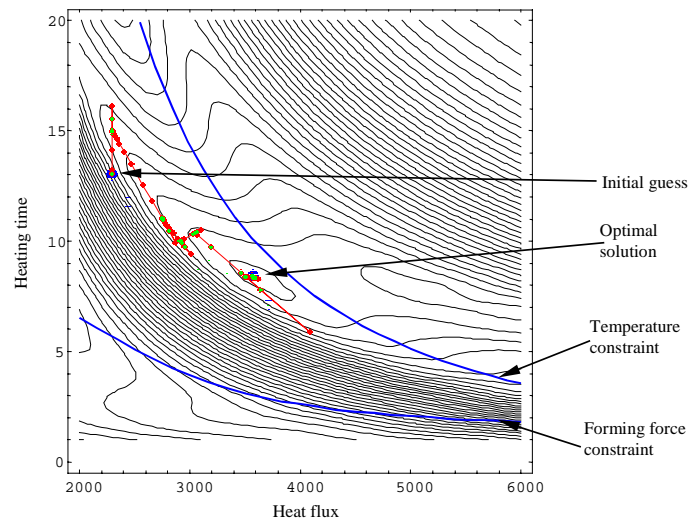
Figure 5.28: Contours of the objective function with temperature constraint and optimal solution.

5.3 Optimal Prestressing of Cold Forging Dies

The final example considered is an industrial case and is related to prestressing of cold forging dies which are subject to low cycle fatigue.

Cold forging dies are subjected to high operational loads which often lead to fatigue failure. To prevent or reduce excessive growth of fatigue cracks the dies are used in a prestressed condition which must be designed in such a way that plastic cycling and tensile stress concentrations in the die are minimised[5],[6]. This can be achieved by optimising the geometry of the interface between the stress rings and die inserts. Prestressing of an axisymmetric die[7]-[9] which can be simulated in two dimensions is considered first. Then a three dimensional prestressing example[13],[14] is presented.

5.3.1   Optimisation of the Geometry of the Outer Surface of an Axisymmetric Die

Prestressing is used in cold forging technology to increase the service life of tooling systems. In conventional approaches the interference between the stress ring and the die insert is uniform resulting in small variations of fitting pressure distributions. However, the introduction of high strength stripwound containers[5] allows relatively high variations of the fitting pressure which can be optimised.
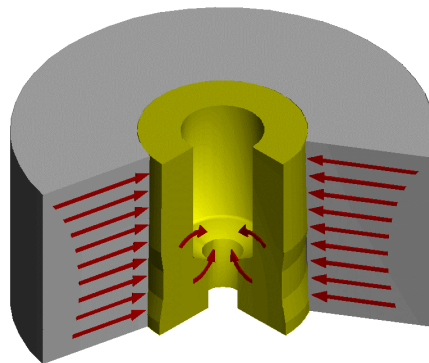
Figure 5.29: Prestressing of the die insert.

In the approach proposed in [6] a non-uniform fitting pressure distribution is obtained by modifying the geometry of the interference which is parametrised as

presented in Figure 5.30. By optimising the position and geometry of the groove it is possible to achieve high compressive stresses in the inlet radius (Figure 5.29) and therefore reduce damage and eventual crack propagation in this critical part of the die insert during use.
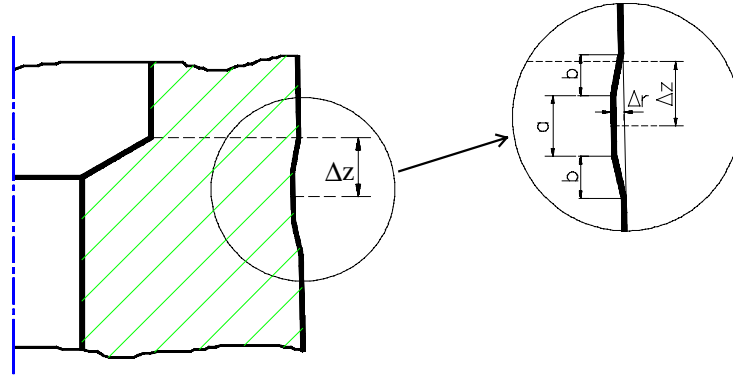
Figure 5.30: Geometric design of the interference at the die-ring interface.

The tooling system was discretised by the finite element method as presented in Figure 5.31. Both the tool and the ring were considered elastic and Coulomb's friction law was assumed at their interface. The prestressed conditions were analysed so that the die insert and the ring overlap at the beginning of the computation. Equilibrium is then achieved by an incremental-iterative procedure by updating the contact penalty coefficient.

Two objectives of the optimisation procedure were applied: to position the minimum of the axial stress acting in the inlet radius close to node 6 (see Figure 5.31) and to make this minimum as numerically large as possible. Optimisation was performed as minimisation of the objective function which was designed to measure the violation of our objectives in the following way:

$$F(a, b, \Delta r, \Delta z) = K \left(f_m(a, b, \Delta r, \Delta z) \right)^2 + \sigma_{zz}^{(6)}(a, b, \Delta r, \Delta z), \qquad (5.26)$$

where $f_m(a, b, \Delta r, \Delta z)$ is a measure of the distance between node 6 and the point on the inlet radius where minimum axial stress is calculated, $\sigma_{zz}^{(6)}(a, b, \Delta r, \Delta z)$ is the axial stress at node 6 and K is a weighting factor which weights the importance of the two objectives. If the second term in (5.26) is omitted, the problem does not have a unique solution. There is more than one set of parameters for which the minimum

axial stress appears exactly in node 6. Therefore the objective function was designed with both terms. The results obtained with $K = 1000$ and $K = 100$ are given in Table 5.11 and Table 5.12, respectively.
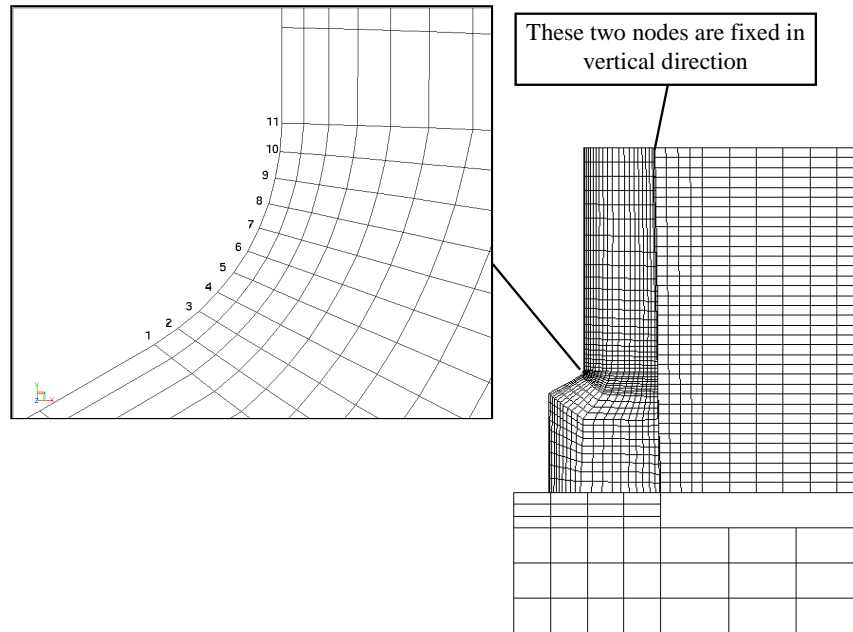
Figure 5.31: Numerical discretisation of the tooling system.

After the optimisation a parameter study has been performed to assess the stability of the problem. It has been found that the problem is well posed, so that the optimisation approach presented can be applied. The only restriction is the initial guess which should be chosen so that the axial stresses in the inlet radius are compressive.

Table 5.11: Results of optimisation with $K = 1000$.

	a [mm]	b [mm]	Δr [mm]	Δz [mm]
Initial guess	6	8	0.3	-4
Final solution	4.97	6.15	0.319	-7.01
Final value of F	-1511			

Table 5.12: Results of optimisation with $K = 100$.

|	a [mm]	b [mm]	Δr [mm]	Δz [mm]
Initial guess	6	8	0.3	-4
Final solution	5.79	7.11	0.308	-5.28
Final value of F	-1855			

5.3.2   Evaluation of Optimal Fitting Pressure on the Outer Die Surface

In the present example the fitting pressure distribution at the interface between the die insert and the stress ring (Figure 5.32) was optimised.

In order to reduce the appearance of cracks, the spherical part of the stress tensor at the critical locations is to be minimised by varying the fitting pressure distribution at the interface between the die insert and the stress ring. The following two constraints were taken into account:

- The normal contact stress distribution at the interface between die insert and stress ring must be compressive.
- The effective stress distribution at all points within the prestressed die must be below the yield stress.

Critical locations
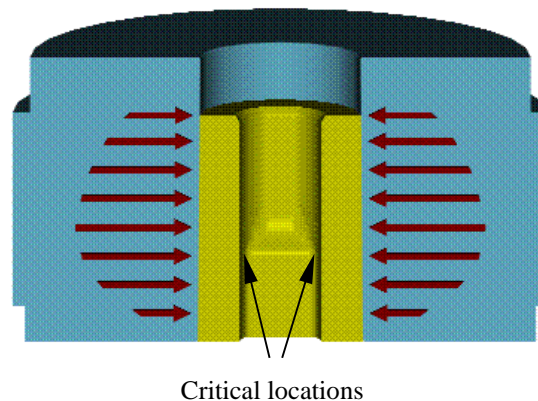
Figure 5.32: A prestressed cold forging die with indicated critical locations where cracks tend to occur.

The fitting pressure distribution was represented by 220 parameters corresponding to a subdivision of the contact surface into 20 vertical and 11 circumferential units A_{ij} (Figure 5.33). Index k which associated the optimisation parameter (i.e. the pressure) p_k with the corresponding A_{ij} is computed as $k = (j-1) \cdot 11 + i$.

Because of symmetry only one half of the die was simulated (Figure 5.33). The objective function was defined as the spherical part of the stress tensor at the critical location, i.e.

$$\theta(\mathbf{p}) = \frac{1}{3}\sigma_{kk}^{crit.}(\mathbf{p}). \qquad (5.27)$$

The first constraint was enforced by using transformations where instead of optimisation parameters $\mathbf{p}$ a new set of variables $\mathbf{t}$ is introduced. The following transformations are applied:

$$p_k = \alpha \frac{g_k}{\sqrt{g_i g_i}}; \qquad g_k = e^{t_k}. \qquad (5.28)$$

In the above equation α is a scalar variable which satisfies the second constraint. Once the optimisation problem is solved for $\mathbf{t}$ the optimal set of parameters $\mathbf{p}$ is derived by using equation (5.28).

Sensitivities of the objective function with respect to optimisation parameters were calculated according to the adjoint method (chapter 3) in the finite element environment, as well as the objective function. They are shown in Figure 5.33. These calculations were used in the optimisation procedure. The obtained optimal pressure distribution is shown in Table 5.13 and in Figure 5.34. Figure 5.35 shows the prestressing conditions and the effective stress distribution for the optimally distributed fitting pressure.

**Table 5.13:** Optimal set of parameters $\mathbf{p}^{opt}$ defining the fitting pressure distribution.

j \ i	1	2	3	4	5	6	7	8	9	10	11
1	93.22	89.60	85.38	82.11	80.36	83.31	92.85	105.13	121.88	136.91	147.27
2	101.00	97.53	90.23	82.95	81.88	87.34	102.07	121.50	151.92	174.00	185.89
3	116.63	103.89	91.26	81.00	77.90	90.44	119.19	160.50	209.39	246.51	270.45
4	129.90	108.10	86.25	66.13	60.13	79.96	135.44	209.61	297.44	357.58	398.65
5	138.26	103.64	64.15	27.40	7.03	43.68	124.26	257.59	409.57	526.52	600.05
6	129.25	85.72	27.50	0.55	0.30	0.58	102.36	328.85	582.39	764.12	859.46

|											
7	99.56	46.61	0.71	0.19	0.13	0.20	104.45	409.26	733.05	977.29	1109.89
8	64.44	4.84	0.28	0.13	0.10	0.19	128.25	468.18	830.35	1113.63	1261.72
9	24.71	0.77	0.24	0.15	0.14	0.58	208.79	532.54	851.79	1117.16	1259.67
10	0.75	0.47	0.30	0.25	0.38	73.55	274.47	556.57	807.61	1007.96	1121.13
11	0.28	0.29	0.28	0.48	19.04	138.51	302.58	506.80	687.32	843.22	915.33
12	0.19	0.21	0.27	0.59	41.78	148.50	282.74	415.76	560.36	661.28	716.32
13	0.16	0.18	0.24	0.51	27.46	118.75	225.14	332.13	424.23	500.06	542.03
14	0.15	0.17	0.22	0.43	6.14	84.16	164.29	246.59	320.54	374.65	403.52
15	0.16	0.18	0.23	0.38	1.75	53.06	116.07	176.89	231.37	270.39	289.37
16	0.18	0.20	0.25	0.39	0.99	27.31	74.64	118.57	156.76	187.19	200.39
17	0.21	0.23	0.28	0.40	0.80	5.40	44.14	73.12	99.67	119.70	132.83
18	0.27	0.29	0.34	0.45	0.71	1.86	12.72	29.81	49.39	65.89	72.32
19	0.36	0.38	0.43	0.51	0.66	0.96	1.54	2.83	6.18	15.27	23.07
20	0.51	0.52	0.54	0.56	0.57	0.62	0.66	0.68	0.69	0.72	0.72
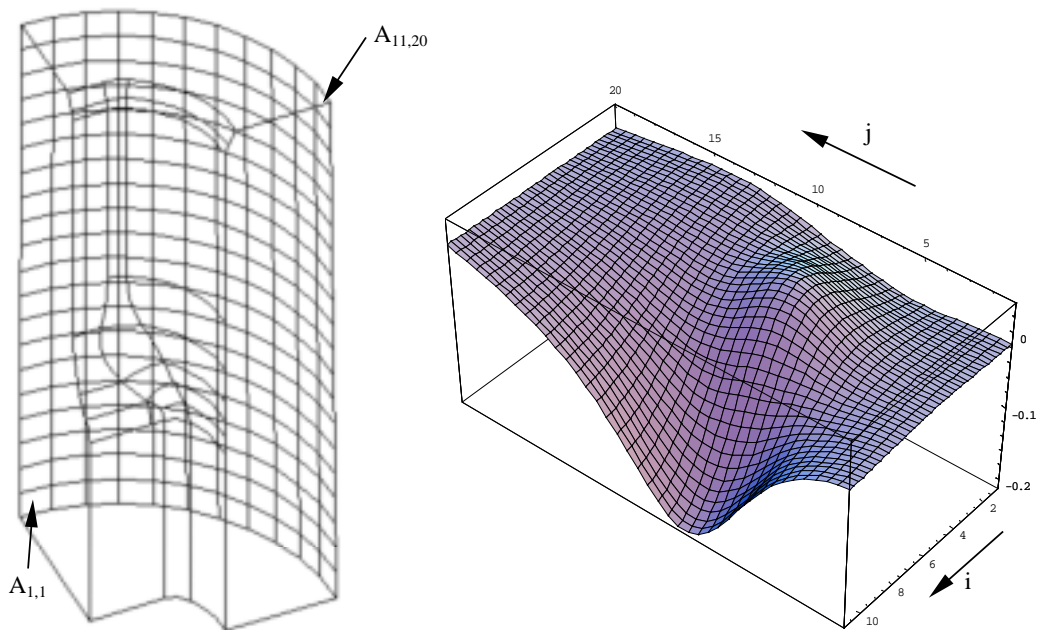
Figure 5.33: Subdivision of the outer surface of the die and sensitivities $D\theta/Dp_k$.
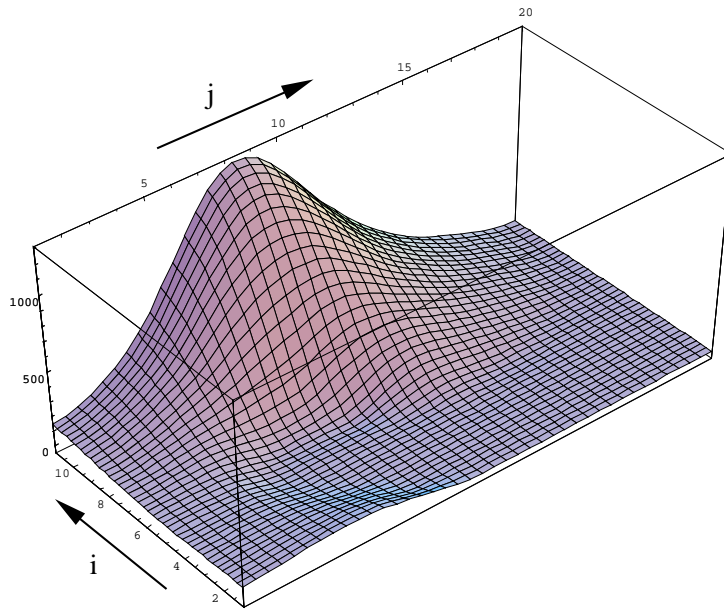
Figure 5.34: Optimal fitting pressure distribution.
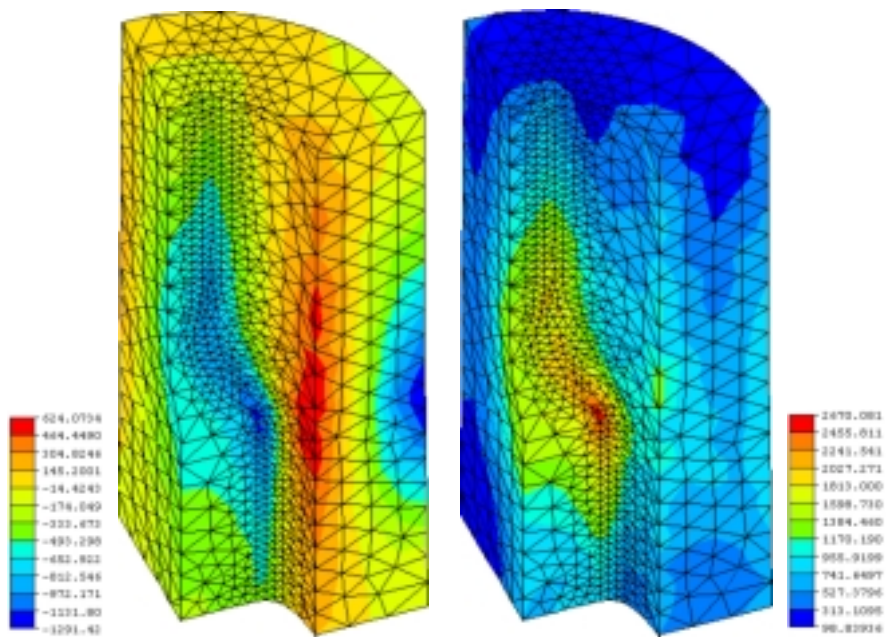
Figure 5.35: Prestressing conditions $\sigma_{kk}/3$ and effective stress distribution for $\mathbf{p}^{\text{opt}}$

5.4 Further Examples

A number of other problems were solved by the presented optimisation shell. In the work done by Musil[15] friction parameters were estimated from the results of the spike forming test (Figure 5.36). A block sample was pressed between two cylinders and a plate. Torque and the two components of the force acting on the cylinders were measured at different stages to provide input for inverse analysis.
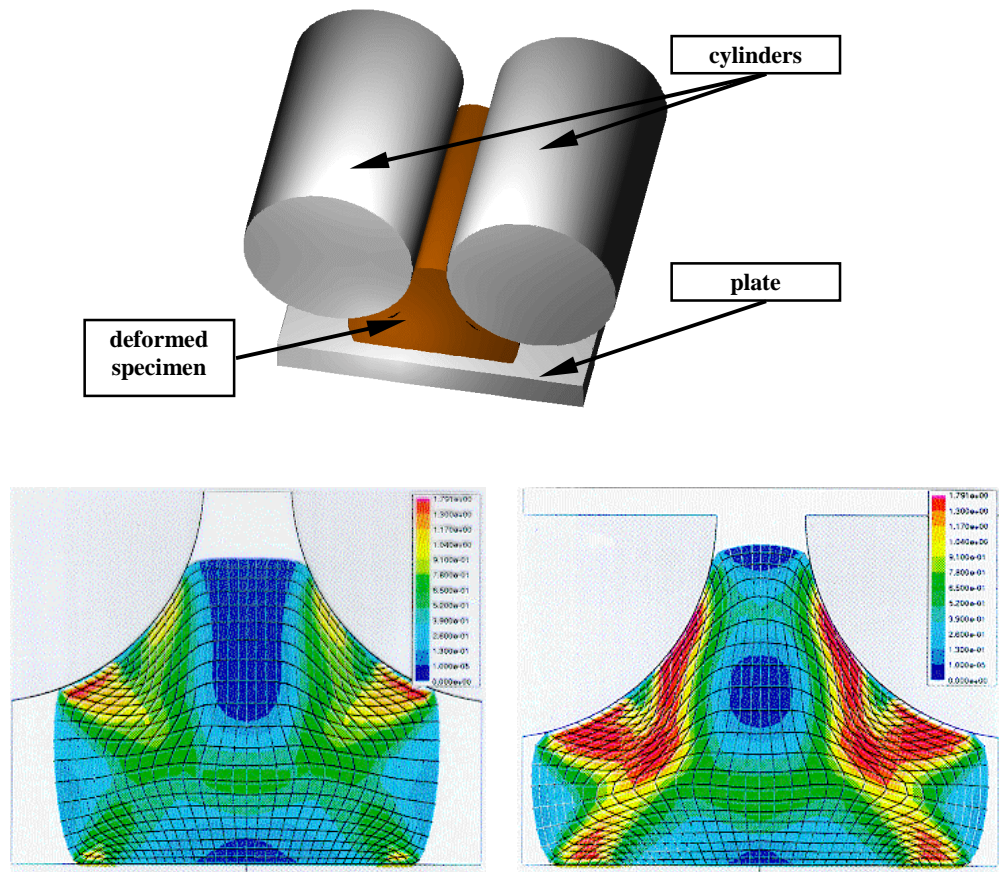

Figure 5.36: Experimental set-up and numerical simulation of the spike forming test.

Another inverse parameter identification is described in the work done by Goran Kugler[16] where the dependence of the heat transfer coefficient between two bodies in contact on the normal contact stress is estimated. A hotter cylindrical specimen was symmetrically pressed by cooler dies. The temperature in a few sampling points within the dies was measured at different times.

These two examples illustrate the applicability of the inverse approach to identification of model parameters which are difficult to estimate by other methods. The parameters of physical models that describe contact phenomena which take place during hot working operations are especially difficult to quantify. Due to high contact stresses and temperatures it is hard to make in situ measurements. It is however possible to design experiments in which conditions similar to those in the real process are reestablished and where accurate indirect measurements can be performed. The estimated parameters can be used to calibrate numerical simulation of the real process.

A shape optimisation example which is close to real-life problems in metal forming was solved by Damijan Marković[19]. A pre-form shape was optimised in order to obtain optimal die filling and material flow. The problem is outlined in Figure 5.37, while the results of a numerical simulation are shown in Figure 5.38.
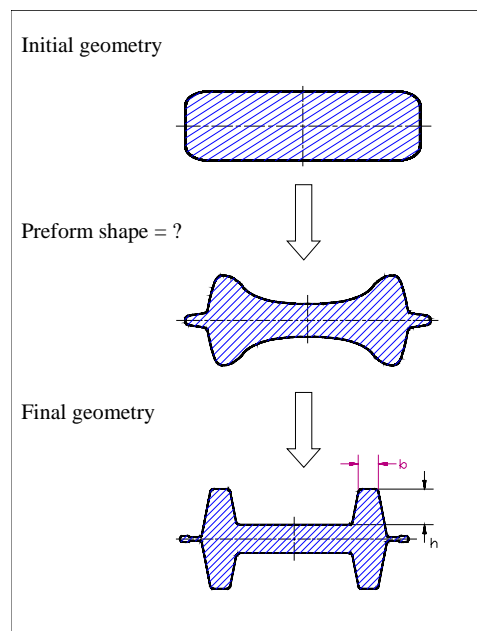

Figure 5.37: Two stage forging process where the pre-form shape is to be optimised.
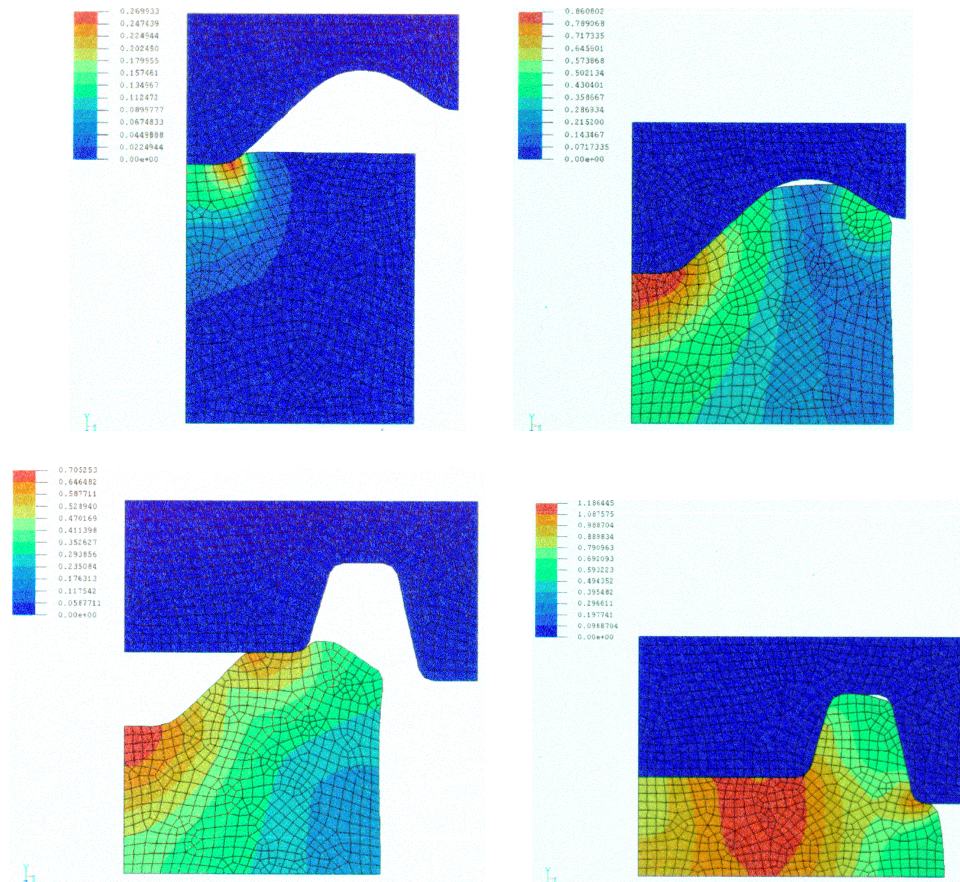
Figure 5.38: Numerical simulation of a two stage forging process.

An interesting example which demonstrates a stand-alone use of the optimisation shell was designed by Jelovšek[18]. Equilibrium arrangements of a given number of equally charged particles in a planar circular region were obtained by minimisation of the total potential energy with respect to particle positions. Different arrangements were obtained by different initial guesses. Expressions defining the objective and constraint functions and their derivatives can be expressed analytically and were evaluated by the optimisation shell. Sample results are shown in Figure 5.39.

w = 382.14

w = 380.51

w = 384.55
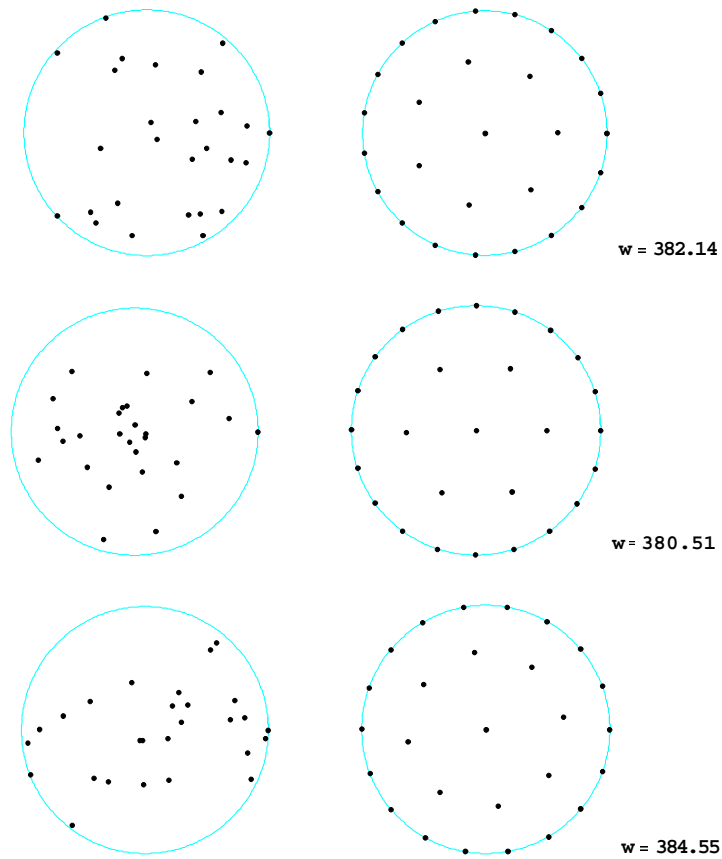
Figure 5.39: Three different equilibrium arrangements of 27 charged particles in a circular region[18]. The corresponding random initial configurations are shown on the left. Relative potential energy of the equilibrium states is indicated on the right.

References:

[1]   G. Dieter, *Mechanical Metallurgy*, McGraw-Hill, Singapore, 1986.

[2]   T. Rodič, I. Gresovnik, D.R.J. Owen, *Application of error minimization concept to estimation of hardening parameters in the tension test*, In: Computational plasticity : fundamentals and applications : proceedings of the Fourth International conference held in Barcelona, Spain, 3rd-6th, April, 1995, Swansea, Pineridge Press, 1995, part 1, pp. 779-786.

[3]   I. Grešovnik, T. Rodič, *Določanje parametrov plastičnega utrjevanja z inverzno analizo nateznega preizkusa* (in Slovene), In: Zbornik del, Kuhljevi dnevi '94, Smarjeske Toplice, 22. - 23. september 1994, Maks Oblak, ur., V Ljubljani, Slovensko drustvo za mehaniko, 1994, pp. 193-198.

[4]   T. Rodič, I. Grešovnik, *Omejevanje zalog vrednosti pri reševanju inverznih problemov z uporabo transformacij* (in Slovene), In: Zbornik del : Kuhljevi dnevi '95, Kuhljevi dnevi '95, Radenci, 21. - 22. september 1995, Maks Oblak, ur., V Ljubljani, Slovensko drustvo za mehaniko, 1995, pp. 231-238.

[5]   J. Gronbaek, *Stripwound Cold-forging Tools - a Technical and Economical Alternative*, Journal of Materials Processing Technology, Vol. 35, pp. 483-493, Elsevier, 1992.

[6]   E. B. Nielsen, *Strip winding - Combined Radial and Axial Prestressing of Cold Forging Die Inserts*, Ph.D. Thesis, Technical University of Denmark and STRECON Technology, 1994.

[7]   T. Rodič, I. Grešovnik, *Optimization of the prestressing of a cold forging tooling system*, In: Inverse problems in engineering : theory and practice : preliminary proceedings of the 2nd International conference on Inverse problems in engineering : theory and practice, Le Croisic, France, 9-14 June 1996. Vol. 2, New York, Engineering Foundation, 1996.

[8]   T. Rodič, I. Grešovnik, *Constraint optimization of the prestressing of a cold forging tooling system*, In: Inverse problems in engineering : theory and practice, 2nd International Conference on Inverse Problems in Engineering, Le Croisic, France, June 9-14, 1996, Didier Delaunay, ur., Yvon Jarny, ur., Keith A. Woodbury, ur., New York, ASME, cop. 1998, pp. 45-52.

[9]   T. Rodič, I. Grešovnik, Anton Pristovsek, Joze Korelc, *Optimiranje prednapetja orodij za preoblikovanje v hladnem* (in Slovene), In: Zbornik del, Kuhljevi dnevi '98, Logarska dolina, Slovenija, 1.-2. oktober 1998, Boris Stok, ur., Ljubljana, Slovensko drustvo za mehaniko, 1998, pp. 145-151.

[10]   T. Rodič, J. Korelc, I. Grešovnik, *Inverse analyses and optimisation of cold forging processes*, In: First ESAFORM conference on material forming, Sophia-Antipolis (France), 17-20 March 1998, [Paris], [S. n.], 1998, pp. 255-258.

[11]   T. Rodič, I. Grešovnik, *Analiza občutljivosti napetostnega polja v prednapetem orodju za preoblikovanje v hladnem* (in Slovene), RMZ-mater. geoenviron., vol. 46, no. 1, pp. 89-94, 1999.

[12]   T. Rodič, I. Grešovnik, *Application of inverse and optimisation methods in cold forging technology* , In: 29th ICFG : plenary meeting, Gyur, Hungary 1996, 8-11th September 1996, Györ, Metal forming group of scientific soc. of Hungarian mech. engineers, 1996, pp. 8.1-10.

[13]   T. Rodič, I. Grešovnik, M. Hänsel, M. Heidert, *Optimal Prestressing of Cold Forging Dies*, in M. Geiger (editor), Advanced Technology of Plasticity 1999: Proceedings of the 6th International Conference on Technology of Plasticity (held in Nuremberg, Germany), vol. 1, pp.. 253-258, Springer, Berlin, 1999.

[14]   T. Rodič, I. Grešovnik, D. Jelovšek, J. Korelc, *Optimisation of Prestressing of a Cold Forging Die by Using Symbolic Templates*, in ECCM '99 : European Conference on Computational Mechanics (held in Munich, Germany), pp. 362-372, Technische Universität München, 1999.

[15]   M. Musil, *Določitev koeficienta trenja z inverzno metodo* (in Slovene), diplomsko delo, University of Ljubljana, 1998.

[16]   G. Kugler, *Določitev koeficienta toplotne prestopnosti z inverzno analizo* (in Slovene), diplomsko delo, University of Ljubljana, 1998.

[17]   D. Jelovšek, *Določitev predoblike pri plastičnem preoblikovanju* (in Slovene), diplomsko delo, University of Ljubljana, 1998.

[18]   D. Jelovšek, *Equilibrium States of Charged Particles in a Two-dimensional Circular Region*, electronic document at http://www.c3m.si/inverse/examples/charges/index.html, Ljubljana, 2000.

[19]   Damijan Markovič, *Optimizacija predoblike pri kovanju* (in Slovene), diplomsko delo, University of Ljubljana, in press.

[20] H. S. Carslaw, J. C. Jaeger, *Conduction of Heat in Solids*, Clarendon Press, Oxford, 1959.

[21] A. Likar, *Osnove fizikalnih merjenj in merilnih sistemov (in Slovene)*, DMFA Slovenije, Ljubljana, 1992.

[22] I. Kuščer, A. Kodre, H. Neunzert, *Mathematik in Physik und Technik (in German)*, Springer - Verlag, Heidelberg, 1993.

[23] E. Kreyszig, *Advanced Engineering Mathematics (second edition)*, John Wiley & Sons, New York, 1993.

[24] W.H. Press, S.S. Teukolsky, V.T. Vetterling, B.P. Flannery, *Numerical Recipies in C – the Art of Scientific Computing,* Cambridge University Press, Cambridge, 1992.